Acoustic Tweezer Modulated Biomimetic Patterned Particle-Polymer Composite for Water Vapor Harvesting

M Shahriar¹, Yu Hui Lui¹, Bowei Zhang², Ketki Lichade³, Yayue Pan³, Shan Hu^{1,*}

*Email: shanhu@iastate.edu

Abstract

With the recent threat of climate change and global warming, ensuring access to safe drinking water is a great challenge in many areas worldwide. Designing functional materials for capturing water from natural resources like fog and mist has become one of the key research areas to maximize the production of clean water. From this aspect, nature is a great source for designing bioinspired functional materials as some of the plant leaves and animal exoskeletons can harness water and then store it to save themselves from arid, xeric conditions. Inspired by the Steno Cara Beetle, we have designed a composite surface structure with periodic islands made of aluminum microparticles surrounded by poly(dimethylenesiloxane) (PDMS). An acoustic tweezer-based method was used to fabricate the bioinspired composite structures, where surface acoustic waves at specific frequencies and amplitudes are applied to align the microparticles as islands in the polymer matrix. An oxygen plasma etching step was applied to expose the microparticles on the PDMS surface. The average water harvesting efficiency for structures made with 120 KHz and 80 KHz acoustic frequencies and one hour etching time were found to be 9.41 gcm⁻²h⁻¹ and 8.84 gcm⁻² ²h⁻¹ respectively. The acoustically-patterned biomimetic composite surface showed higher water harvesting efficiency compared with completely hydrophobic PDMS and hydrophilic aluminum surfaces, demonstrating the advantages of the bioinspired composite material design and acousticassisted manufacturing technique. The biomimetic fog water harvesting material is a promising avenue to fulfill the demand for a cost-effective, sustainable, and energy-efficient solution to safe drinking water.

Keywords: Biomimetic, Acoustic tweezer, Polymer composites, Wettability, Water harvesting.

1. Introduction

Water is the most substantial liquid material on earth and blessings of nature. All the living beings on earth live on drinking water and lack of a certain amount of water in our body cause serious dehydration that can lead to death. The unavailability of water in desert and some drought regions

¹ Department of Mechanical Engineering, Iowa State University, Ames, Iowa 50011, United States

² School of Mechanical and Power Engineering, East China University of Science and Technology, Shanghai, 200237, China

³ Department of Mechanical and Industrial Engineering, University of Illinois Chicago, Chicago, Illinois 60607, United States

on earth all year round makes life extremely difficult for the inhabitants. Specially, scarcity of adequate drinking water causes serious consequences during summer¹⁻². A sustainable technology that can mitigate the shortage of fresh water is a prime concern for engineers. Apart from that, recent climate change and global warming that cause temperature increment and imbalance in weather have fueled up the issue to a great extent and added more concern³⁻⁷. Though there are some recent technologies such as desalination and filtration plants in market, more cost-effective and efficient methods are still needed for water security of our society. From this perspective, the focus of developing new technology has now shifted to the design and manufacturing of new materials, among which composite polymer surfaces show encouraging performances when utilized to harness water from the atmosphere⁸⁻¹¹.

Nowadays, bioinspired design of nanocomposites has drawn attention of researchers due to the ability to mimic the properties of the specific biological plants or animals. For instance, in nature, some animal exoskeletons and plant leaves have astonishing property of collecting water from the environmental mist and can store it for future use. Particularly, Nami Dessert beetle can harness water from the ambient humid weather. Their exoskeletons consist of an array of hydrophilic bumps on top surface and a hydrophobic background that is immediately beneath the bumps. The array of bumps facilitates the condensation of water as droplets from the mist or fog laden air and holds them on the surface due to the hydrophilic property. The hydrophobic background helps the coalesced droplets roll off the surface. Inspired by this property, many 2D wettable surfaces for water harvesting have been developed adopting different synthesis techniques. Nevertheless, there is still a need for water harvesting materials with high efficiency, low cost, low energy consumption, and facile manufacturing 12-17.

Zhu et. al. has summarized the four existing fabrication methods for the beetle-inspired composite surfaces: mixing method, responsive method, mask-based method and inkjet printing method¹⁸. 'Mixing method' usually laminates the pre-patterned hydrophilic and hydrophobic layers using thermal pressing¹⁹. The materials used should sustain the thermal pressing temperature/stress and have similar thermal expansion coefficients to avoid delamination. Also, this method is not particularly viable for making composite surface with thermosets. In 'responsive method' the patterning process should be triggered by some stimuli such as light irradiation, temperature, electric potential, which limits the choice of materials to only those that are responsive to the stimuli. The 'mask based method' process is very complex and lengthy as it requires multiple steps such as mask preparation, mask transfer, mask alignment, etc. Moreover, the use of masks increases the manufacturing cost because the masks need to be replaced regularly to avoid cross contamination and loss of patterning accuracy. In 'inkjet printing method', the printing inks are required to be jetable, which limits the use of viscous materials. In addition, to prevent clogging of the inkjet printing nozzle, the particles in the printing inks needs to be submicron sized and surfactants are usually added to the inks to prevent agglomeration of the particles. These surfactants will significantly affect the surface wettability of the printed structure and might play a negative role in creating a wettability gradient needed for the water vapor harvesting.

Acoustic tweezer is a a noninvasive and contactless method to manipulate particles on any solid plate or dispersed inside the polymer matrix ²⁰⁻²². In this paper, a facile method based on acoustic tweezer has been developed for the fabrication of the beetle-inspired composite surfaces. In our acsoutic tweezer, surface standing acoustic wave was generated by piezoelectric transducers, propagated along a Kapton polymer substrate as antisymmetric lamb wave, and finally leaked into the liquid media to assemble the particles into desired pattern. For our experiment, the liquid media

is PDMS in toluene solution and the particles are aluminum (Al) microparticles. The Al microparticles clustered at the acoustic pressure nodes as islands surrounded by PDMS. After the PDMS was cured, an oxygen plasma etching step was applied to futher expose the Al microparticle islands on the PDMS surface. The as-obtained composite film with hydrophilic Al bumps surrounded by hydrophobic PDMS valleys mimics the exoskeleton structure of the dessert beetle and demonstrates promising water vapor harvesting performance, compared with other water-harvesting films fabricated by more complex methods^{18, 23-25}.

Compared with existing methods to fabricate the bio-inspired composite surface, the acoustic tweezer-based process puts fewer restrictions on the materials properties: it only requires there is density difference between the particles and their surrounding media (e.g. the polymer solution), which can be more easily satisfied than the requirement on material's electrical, magnetic, optical, thermal properties ²⁶⁻³⁰. Further, acoustic patterning has been achieved in low-viscosity colloidal solution as well as highly viscous composite polymer solution ³¹⁻³³. It can also precisely pattern particles with sizes ranging from nanometers to millimeters even without the need to suppress agglomeration with surfactant ³¹⁻³⁵. In short, the most significant advantage of acoustic tweezer-based method compared with other methods is the unbeatably wide range of materials it can work with. Moreover, the acoustic particle patterning is also highly scalable. Depending on the size and number of the acoustic actuators used, particle patterns have been achieved over areas ranging from several mm² to hundreds of cm² ³⁶⁻⁴⁰.

2. Working mechanisms of acoustic patterning of particles in liquid media

Once the particles are stabilized in the stagnant liquid media, they can randomly move due to the Brownian motion or can be diffused due to the chemical potential. When a standing acoustic wave is established in the liquid, the acoustic radiation force (F_r) exerted on a spherical particle in the non-viscous liquid can be described by Equation 1^{41} .

$$F_r = \frac{2\pi V_P E_{ac}}{\lambda} \Phi \sin(\frac{4\pi x}{\lambda}) \tag{1}$$

Where V_P is the volume of the particle, λ is the wavelength, x is the transverse particle path, Φ is the acoustic contrast factor, E_{ac} is the acoustic energy given in Equation 2:

$$E_{ac} = \frac{p_a^2 \beta_f}{4} \tag{2}$$

Where, p_a is the acoustic pressure and β_f is the compressibility of the fluid.

At the same time, while travelling in the liquid, the particles also experience Stokes drag force induced by acoustic streaming which is given by Equation 3 ⁴².

$$F_d = 6\pi\mu r v_p \tag{3}$$

Where, μ is the dynamic viscosity of the liquid and v_p and r are the velocity and radius of the particle respectively.

Previous study has shown that for acoustic radiation force to dominate over the acoustic streaming induced drag force, the size of the particle should be larger than 2 μ m and the viscosity of the fluid needs to be low ⁴³. The lower viscosity reduce the undesireable drag force which will help pattern the particles with low acoustic power. For this reason, in our experiment we have to optimize the

viscosity of the PDMS solution by adjusting the PDMS to toluene ratio and the best ratio was found to be 50% W/W. With the adjusted viscosity, we have achieved high-quality particle patterns even with low acoustic power input.

The acoustic radiation force will drive the particles towards the pressure nodes or antinodes depending on the acoustic contrast factor Φ given in Equation 4:

$$\Phi = \frac{5\rho_{\rm p} - 2\rho_f}{2\rho_{\rm p} + \rho_f} - \frac{\beta_p}{\beta_f} \tag{4}$$

 $\Phi = \frac{5\rho_{\rm p}-2\rho_f}{2\rho_{\rm p}+\rho_f} - \frac{\beta_p}{\beta_f} \eqno(4)$ Where, $\rho_{\rm p}$ is the density of the particle and ρ_f is the density of the fluid and β_p is the compressibility of the particle. Acoustic contrast factor determines the equilibrium position of the particles: if $\Phi > 0$, the microparticles will aggregate at the pressure nodes, otherwise at the pressure antinodes.

3. Materials and methods

3.1 Preparation of PDMS and Al microparticle mixture

To prepare the polymer solution, the PDMS (Sylgard 184, Dow Corning) part-A and part-B were first mixed with 10:1 v/v ratio. After that, 5g of toluene (Fisher Scientific) was added into the 5g of PDMS-curing agent mixture and stirred vigorously until the PDMS was completely solvated. Al particles (Alpha Chemicals) with 30 µm size were dispersed in the solution as 1 wt% of the total 10g solution and stirred vigorously until a homogeneous mixture was obtained.

3.2. Acoustic tweezer-based particle manipulation

Schematic of the acoustic tweezer-based particle manipulation platform is shown in Figure 1(a). For the acoustic tweezer, piezoelectric ceramic plates (Steminc Inc.) with the dimension of 20x15x1.4 mm and resonant frequency of 1.5 MHz were used as the piezoelectric transducers (PZTs). The PZTs were coupled to a Kapton film (McMaster Carr) of dimension 80x80x0.075mm using vacuum grease (Dow Corning). Figure 1(a) also shows the wiring connection of the PZTs with the function generator and amplifier to adjust the frequencies and amplitudes of the acoustic waves. As shown in Figure 1(b), a 3D printed structure has been developed to hold the PZTs in a rectangular housing and the PZTs were placed along the diagonal lines of the square substrate. Another 3D printed squre structure (Figure 1(c)) was placed on top of the Kapton substrate and worked as vat to hold the PDMS/Al particle mixture. Object260 CONNEX 3D printer was used and Vero whiteplus photopolymer was chosen for the 3D printed structure as it does not react with the PDMS or toluene. SEM and EDS were performed using FEI Inspect 50 SEM.

3.3. Acoustic tweezer assisted fabrication of the biomimetic composite surface structure

The flow chart in Figure 1(d) has shown the step-by-step procedures to fabricate the biomimetic composite surface structure using acoustic tweezer based particle patterning. First, 10 g of the PDMS/Al mixture was pour into the vat. To generate islands of Al particles for the biomimetic design, two adjacent PZTs were connected to the amplifier without output voltage (peak-to-peak) and output frequencies of 80 KHz, 160V and 120 KHz, 80V respectively. The other two PZTs remained inactive and worked as uniform solid boundary layers to form stadnign acoustic wave. The whole setup was kept standstill to allow the Al particles to precipitate at the bottom and allow toluene to evaporate under room temperature. Then the patterned solution was transferred to an oven and thermally cured at 65 °C. The cured film was peered off from the Kapton substrate and the surface of the film that is adjacent to the Kapton substrate was treated with oxygen plasma etching to expose the aluminum microparticles over the PDMS surface. The etched surface was further examined a confocal microscopy VK-X3000 series 3D surface profiler (Keyence).

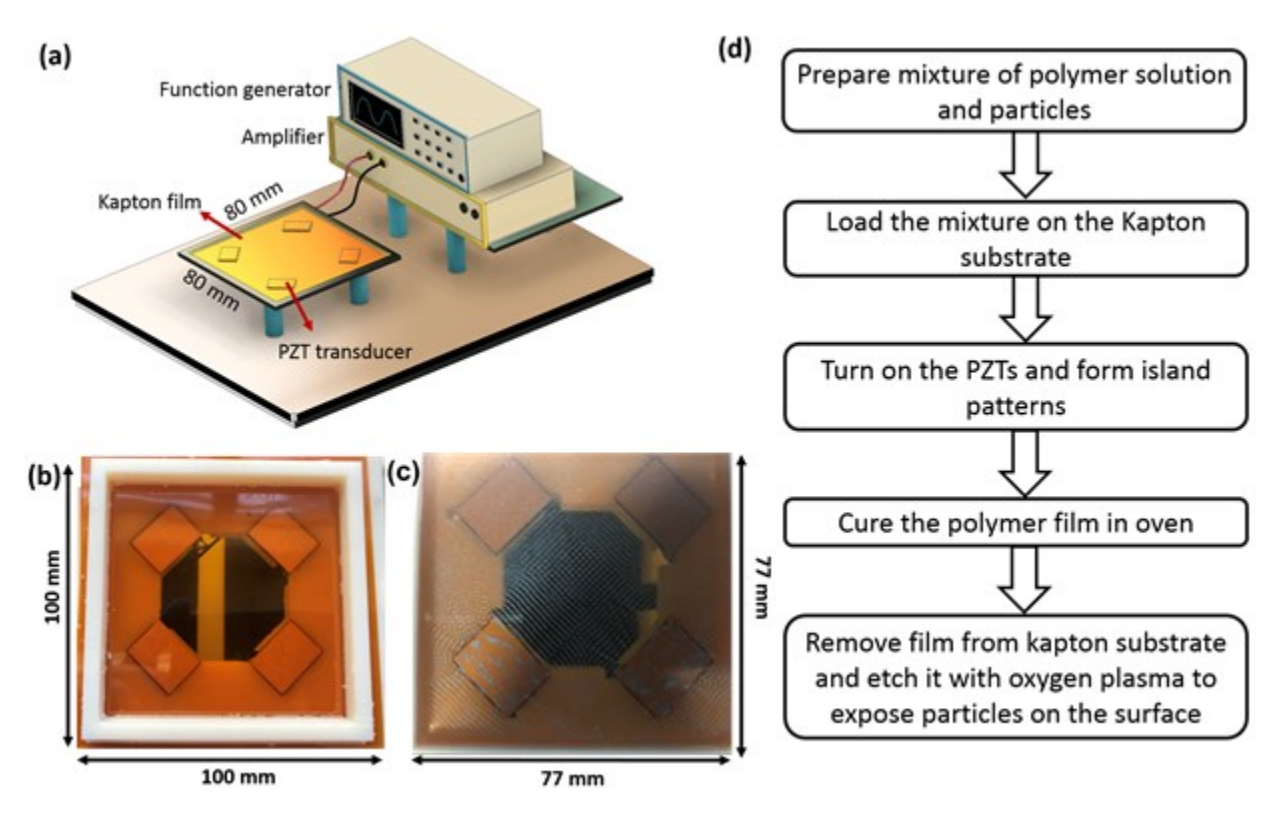


Figure 1: Schematic of the step-by-step procedure to develop the patterned particle composite film fabrication for water vapor harvesting (a) Wiring of the PZTs, (b)3D printed chamber with the kapton substrate (c)Pattern formation after the PZTs are turned on (d) Flow chart showing the method.

3.4. Numerical analysis of standing surface acoustic wave in acoustic tweezer

The PZT transducer can vibrate at large range of frequencies from KHz to MHz (10 KHz-1.5 MHz used in the experiment) but not all frequencies can produce pressure distribution that would generate the islands of microparticles inside the viscoelastic liquid domain. For this purpose, we have conducted numerical simulation of the standing surface acoustic wave with a wide range of frequencies from 40 KHz to 180 KHz to determine the input frequencies for the generation of particle islands. COMSOL Multiphysics was used to run the simulation. The physical domain consists of four PZT plates placed on the two diagonal lines of a square Kapton substrate, as well as the liquid suspension containing Al microparticles as shown in Figure 2(a). The Kapton film dimension was kept 77x77 mm with the thickness of 0.075 mm. The dimension of the each PZT plate was kept as same obtained from the manufacturer with 15x20 mm. Here in the simulation, two adjacent PZTs were utilized to generate the incident acoustic waves and the other two opposite adjacent PZTs were kept as solid uniform boundary wall to form the standing acoustic wave inside the fluid domain. To solve this Multiphysics problem, solid mechanics, pressure acoustic frequency domain and electrostatics module were used, and Multiphysics coupling was adopted to solve the study in two steps. At first, the Piezoelectric Effect Multiphysics solved the interfaces for electrostatics and solid mechanics. Second, the acoustic-structure interaction solved for the

solid mechanics and pressure acoustic interfaces which simulated the leaky wave propagating from the Kapton surface to the PDMS fluid domain. For the pressure acoustics analysis, the boundary conditions for the edges of the Kapton were considered as the 'Prescribed displacement' and the two inactive PZTs were considered as 'Solid hard boundary wall'. To simulate the vibration of the PZT plate, voltage of 80 V was applied to the bottom of the two PZTs and the top parts were set to ground. The 'charge conservation, piezoelectricity' physics converts the applied voltage to the thickness-mode vibration working along Z-axis. 'Frequency domain' analysis was carried out to simulate the acoustic pressure distribution.

4. Result and discussions

4.1 Multiphysics simulation results of the acoustic tweezer

Figure 2(b-f) show the acoustic pressure distribution inside the PDMS under input frequency of 80 KHz, 110 KHz, 120 KHz, 150 KHz and 160 KHz respectively. The bright regions are the pressure nodes and the dark regions are the pressure antinodes. With a positive acoustic contrast factor ($\Phi > 0$), the Al particles always try to aggregate and remain as cluster in the nodal regions. As a result, to form islands of particles, pressure nodes surrounded by four pressure antinodes need to be generated inside the PDMS. As shown in the simulation results, desirable acoustic pressure distribution with high pressure gradients (i.e. higher contrast) between nodes and antinodes are achieved at the center of the Kapton substrate at 80 and 120 KHz. High acoustic pressure gradient means large difference in pressure levels between the pressure node and antinode, which results in better particle pattern quality. Based on the simulation results and analysis, it is conspicuous that, 80 KHz and 120 KHz will generate better pattern quality compared with other frequencies, which supports the choice of these two frequencies for the fabrication of biomimetic composite surface structures with hydrophilic islands surrounded by hydrophobic valleys.

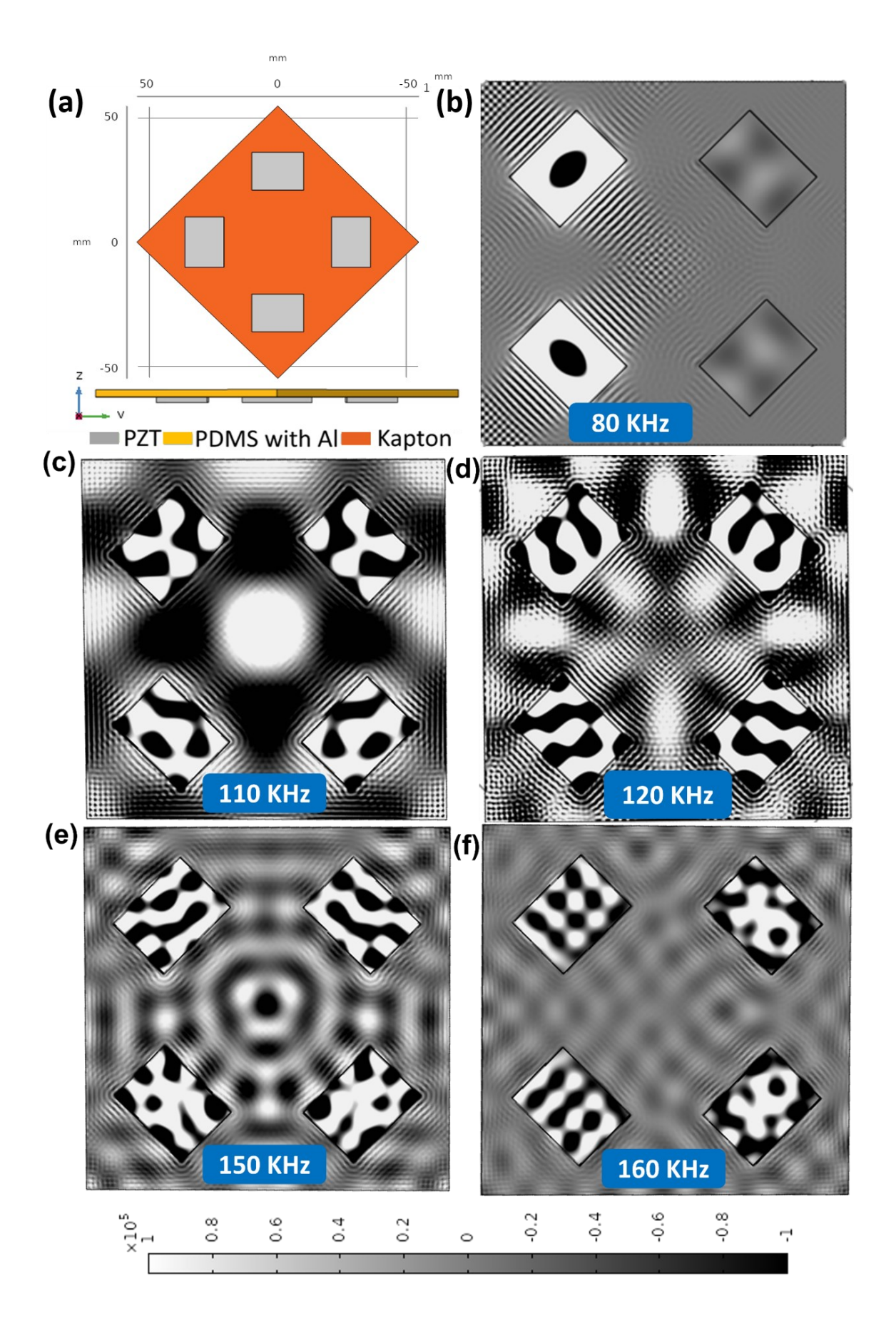


Figure 2: COMSOL Multiphysics simulation of acoustic tweezer for design of input frequency (a) Domain of the physics; Acoustic pressure distribution inside PDMS when input frequency of (b) 80 KHz (c) 110 KHz (d) 120 KHz (e) 150 KHz (f) 160 KHz.

4.2 Structural characterization of the biomimetic composite surface structure

Figures 3(a-b) show the island patterns obtained experimentally from the 120 KHz and 80 Khz input frequencies. To validate the simulation results, we have compared the average distance of four adjacent islands forming the quadrilateral (Figure 3(c-d)) obtained from both simulation and experimental results. For 80 KHz sample, the average distance from the experiment and simulation is 1.496 mm and 1.364 mm respectively. On the other hand, for 120 KHz sample, the average distance from the experiment and simulation is 1.217 mm and 1.186 mm respectively. The results also indicates that, with higher input frequencies, the distance between each island will decrease and number of island patterns per unit area will increase, which has a potential influence in water vapor harvesting efficiency as discussed in next section.

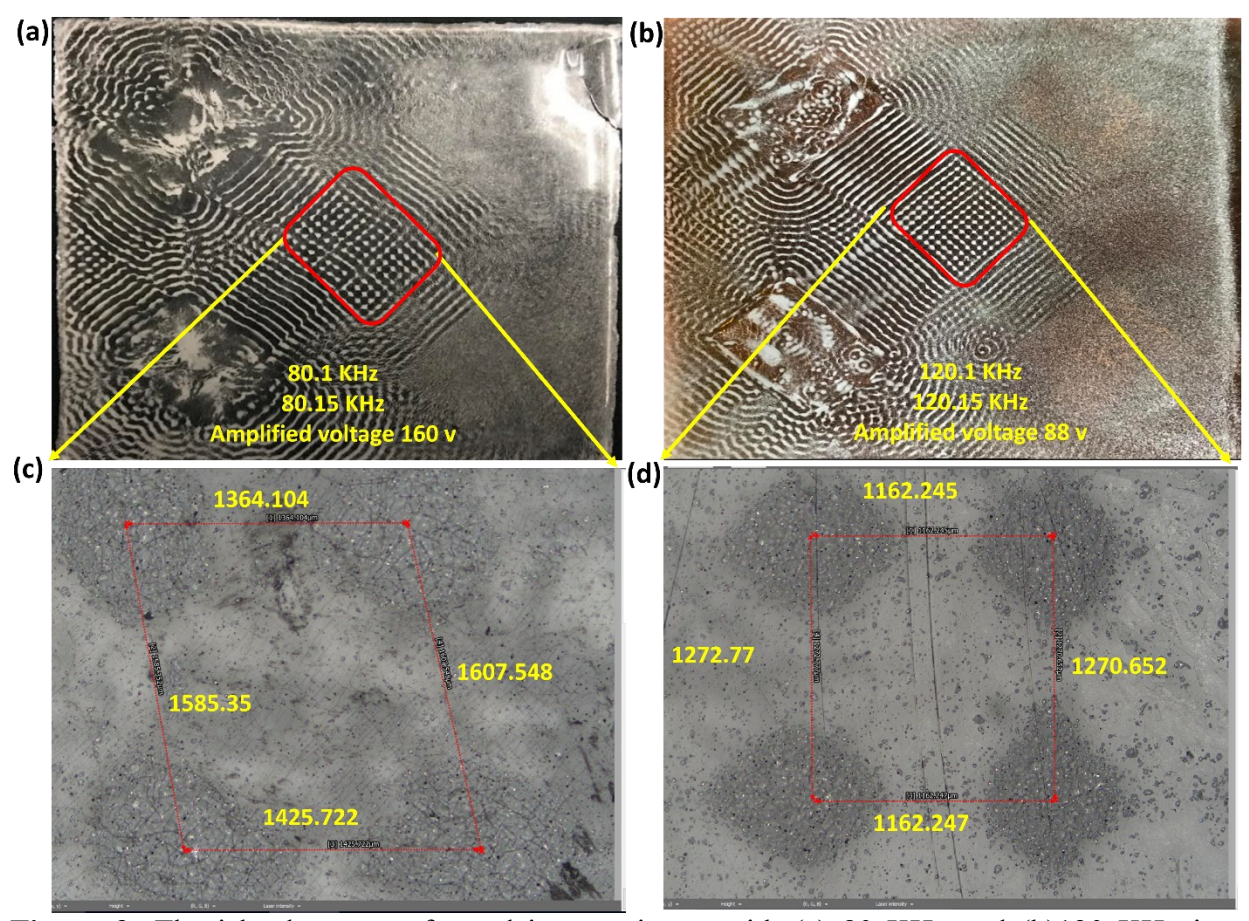


Figure 3: The island patterns formed in experiment with (a) 80 KHz and (b)120 KHz input frequencies and comparison of the distances among the islands forming quadrilateral for (c) 80 KHz sample, (d) 120 KHz sample (the distances shown is in μ m)

The confocal microscopy characterization of the composite surface structure was performed to confirm that the Al microparticles were exposed on the top surface of PDMS film after the oxygen plasma etching step. Oxygen plasma is a chemically reactive process whereas oxygen gas reacts

with hydrocarbon monolayer to form gaseous products and ashes that are swept away as the chamber is always under vacuum pumping process. The heights of the exposed islands from the flat surface were analyzed for different etching time. For this purpose, we have chosen a 80 KHz sample as shown in figure 4(a) and have taken the data for etching time of 40 minutes, 1 hour, 1.5 hours, 2 hours and 2.5 hours. The data were observed by analyzing the six islands over different region to get the average height. Figure 4(b-c) show the confocal imaging of one island and the corresponding 3D surface profile respectively. Finally, to understand how etching time affect the surface profile of the film we have calculated the arithmetical mean height for the island patterns exposed on surface of samples subjected to different etching time. The arithmetical mean height for six islands is summarized in Figure 4(d) and tabulated in Table S1 (Supporting information). For one hour etching time, the average height of the islands is the highest at 0.863 µm, which means there is the maximum exposure of Al particles on the top of PDMS. It is hypothesized that when excessive etching time is used, Al particles might be removed from the PDMS matrix leaving behind dents, which is not helpful for water harvesting. The decreasing water harvesting efficiency from samples subjected to 2.5 hours of oxygen plasma etching supported this hypothesis as discussed further in the Section 4.3. Based on this analysis, the optimized etching time was considered to be 1 hour.

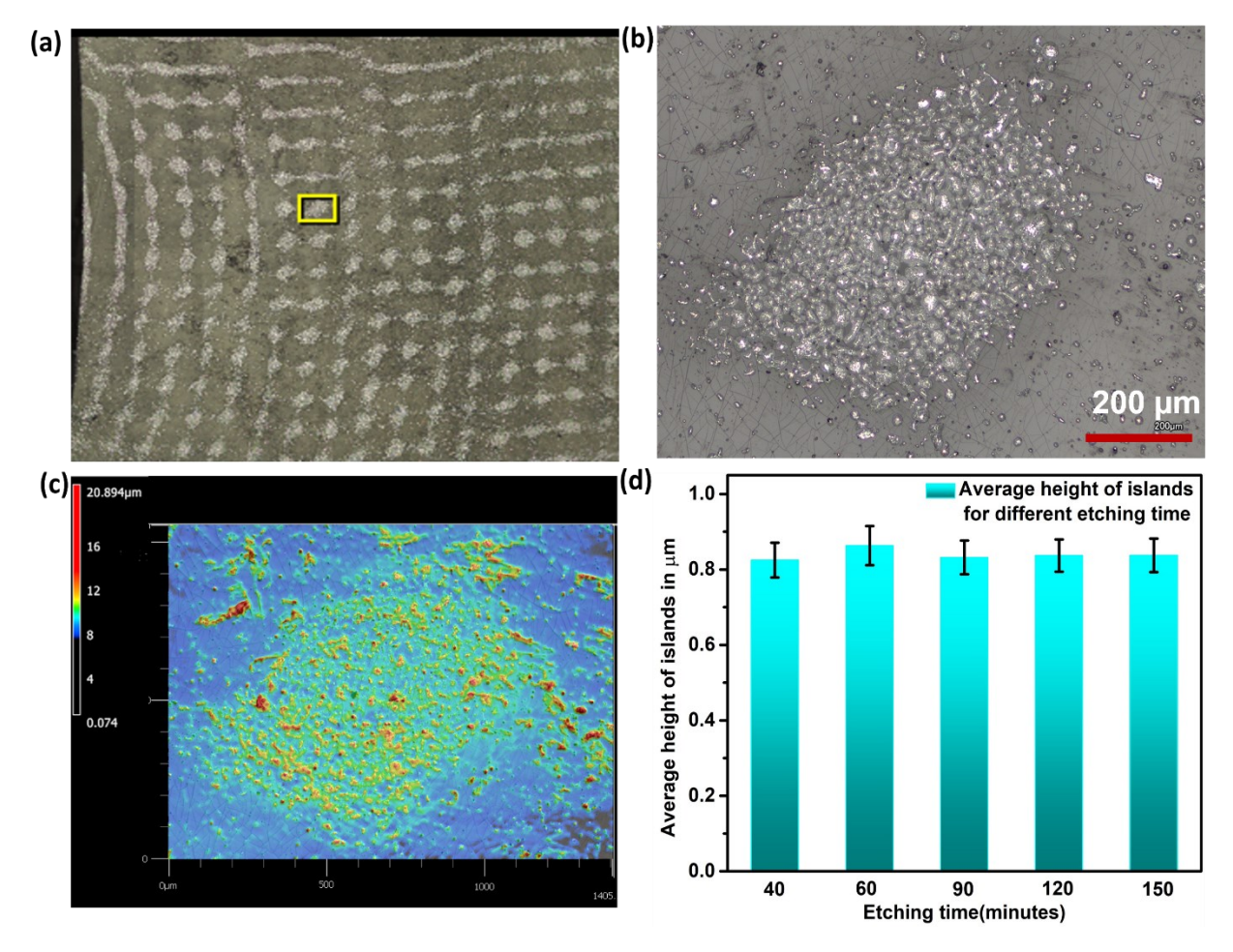


Figure 4: Confocal microscopy characterization of samples subjected to different etching time. (a) Representative samples used for characterization fabricated with input frequency of 80 KHz (the average distance between islands is ~1.5 mm for reference of dimensions); (b) Laser confocal

image of one representative island with the cluster of Al microparticles (c) Height profile of the island using 30% laser confocal (d) Comparison of the arithmetical mean height of the island patterns for samples subjected to different etching time.

4.3. Characterization of water vapor harvesting efficiency

Films with the dimension of 1.2cm x 2cm were used to characterize their water harvesting efficiency. The films were obtained from the middle portion of the PDMS@Al composite films where the island patterns were generated by the acoustic tweezer as shown previously in Figure 3(a-b). Each sample was subjected to etching time of 40 minutes, 60 minutes, 90 minutes and 120 minutes respectively. The water harvesting efficiencies of these samples were measured using a setup built in house (Figure 5(a-b)). Specifically, a fog generator was set at the maximum distance such that beyond this distance the vapor does not reach the surface. The composite film was set vertically with the help of a chemical stand. The whole experiment was conducted inside the fume hood to reduce the omnidirectional air flow. The temperature was kept 72 °F throughout the experiment. The local relative humidity was initially about 16% and after the experiment began, reached the highest level of 32%. A petri dish was placed under the composite film to collect the water droplets rolling down the film and the volume of the collected water was measured for the calculation of water harvesting efficiencies. To demonstrate the benefits of biomimetic design, the water harvesting efficiencies of the hydrophilic Al foil surface and the hydrophoblic PDMS surface were also measured using the same setup.

The water harvesting efficiency is calculated based on the equation below:

$$\eta = V/St$$

where V is the volume of the collected water, S is the vapor capture area or the area of the sample and t is the collection time.

The water vapor harvesting process can be divided into three basic steps: 'Capturing', 'Collection' and then 'Transportation'. During 'Capture', water droplets that are propelled by the wind, come into direct contact with the solid surface. The capturing efficiency is dependent on direction of wind flow, wettability gradient [5], the morphological structures of the surfaces. Even though the tiny water droplets are captured on the surface, there is a possibility the droplet can be evaporated due to wind. So, 'Collection' step is crucial for efficient water vapor harvesting. During collection, the droplet dynamics on the hydrophilic-hydrophobic patterned surface depends on the contrast of the droplet wettability whereas an imbalance force is produced to drive the water droplet from the more hydrophobic to the more hydrophilic region ⁴⁴⁻⁴⁶. The driving force can be written as:

$$F_1 = \gamma(\cos\theta_1 - \cos\theta_2) \tag{5}$$

Where, γ is the surface tension of water and θ_1 and θ_2 are the water contact angles (CAs) on the hydrophilic pattern and hydrophobic substrate respectively. As $\theta_1 < \theta_2$, $F_l > 0$, which means F_l will drive the water droplet to the hydrophilic pattern.

Hydrophilic area generates large pinning force (F_2) due to the capillary force, which is detrimental to water transportation and can be expressed as:

$$F_2 = \gamma L_1(\cos\theta_3 - \cos\theta_4) \tag{6}$$

Where, L_1 is the length of the contact line of a water drop on the hydrophilic area and θ_3 and θ_4 are the receding and advancing CAs respectively.

Meanwhile, as the droplet volume becomes larger after coalescence, the droplet rolls off from the surface when the gravitational force (F_3) grows larger than the pinning force F_2 .

$$F_3 = mgsin \propto -F_2 \tag{7}$$

Here in equation 7, the roll off of droplet occurs when the weight component mgsin \propto is greater than the pinning force F_2 . \propto is the tilt angle of the surface from vertical Z axis. For our case, $\propto =90^{\circ}$, as the surface stands vertically.

From surface characterization it is found that the advancing and receding contact angle on the patterned composite surface (120 KHz and 1 hour etching) are 104° and 82° respectively, which means a positive F_2 is developed to pin the water droplets on the surface based on equation 6 until the gravity of the droplet overcomes the pinning force and the droplet rolls off the surface based on equation 7.

Figure 5(c) shows the water harvesting efficiency of the biomimetic composite surfaces made with different etching time. To analyze the data, we have chosen samples subjected to four durations of etching time for both 80 KHz and 120 Khz frequiencies. For each of the sample, five measurements of water harvesting efficiency were taken over more than three weeks to check the consistency and stability of the sample for long term water harvesting. The same results are also tabulated in Table S2-3 in the Supporting Information. Among the composite surfaces, samples made with 120 KHz input frequency show consistently higher performance than those made with 80 KHz when subjecting to the same etching time ((Table S2 & S3). From table S2 and S3, it is also found that, with one hour etching time the efficiency of water harvesting are higher than other etched samples at same frequency. With 120 KHZ input frequency, the average distance between Al islands is smaller than that at 80 KHZ, hence the number of islands per unit area increases. The observed increase of water harvesting efficiency as the number of islands in the specific area increases is consistent with previous studies ²³. With decreased distance between the hydrophilic islands, it takes less time for the droplets that condense at the hydrophobic region to move to the hydrophilic region. Consequently, the droplets on the Al islands can grow faster to the critical size for rolling off and the water harvesting efficiency is improved. From table S2 and S3, it is also noted that, each of the sample shows gradual decrease of water harvesting efficiency over three weeks. Since the samples did not operate in a clean room, the possible reason for the reduced efficiency is the accumulation of airborne particles on the entire composite surface, which will reduce the wettability gradient critical and thus the water harvesting efficiency. In future work, water harvesting surface with self-cleaning capability needs to be investigated to slowdown the aging of efficiency.

On the other hand, the water harvesting performance slightly varies for samples made with the same frequency but subjected to different etching time. This is possibly due to two reasons. First, plasma etching helps exposed more Al particles to the surface, which enhances the water harvesting efficiency by increasing the contrast of the droplet wettability between the Al islands and PDMS substrate. We have performed SEM and EDS characterization on the samples before and after etching. The Al particles can be observed in the SEM image (Figure S1) EDS elemental mapping (Figure S2) shows that more Al contents can be detected from the sample after plasma etching. Second, prolonged plasma etching will generate cracks on the composite surface, which

will disrupt the water condensation and the droplet transport and hence reduce water harvesting performance. SEM images of the composite surfaces without etching and with prolong 2-hour etching are shown in Figure S3. Without etching the surface is smooth and crack-free, while with prolonged etching, many cracks can be observed on the surface. This crack formation due to plasma etching has also been reported in literature ⁴⁷. In summary, plasma etching is a double-sided sword for the water harvesting performance of the composite surface and there exist an optimal etching time for achieving the best water harvesting efficiency. Among the etching time used in our experiments, 1 hour etching is found to produce samples with the highest water harvesting efficiency as shown in Figure 5(c).

As shown in Figure 5(d), the water harvesting efficiencies of the hydrophilic Al foil surface and the hydrophobic PDMS surface are much lower than those of the composite surfaces. Such stark differences in water harvesting performance demonstrate the advantages of the biomimetic composite surfaces and can be explained by the mechanism of water vapor harvesting on the composite surfaces and the droplet dynamics during the process. If the whole sample is hydrophilic (such as Al foil), the water droplets form a film that covers the whole surface and adheres to it due to the strong adhesion force. This phenomenon would hinder the process of collecting additional water droplet and thus deteriorating the condensation on the surface as there is no dry area left. On the other hand, for the PDMS surface with no Al particles, the hydrophobic surface allows the formation of water droplets but lacks the hydrophilic properties that facilitate the droplet coalescence. Without coalescence, the water vapor harvesting is also limited, because the size of the water droplets formed on the PDMS surface remain small, which means droplet roll-off due to gravity is relatively difficult and water evaporation is relatively fast compared with larger droplets formed by coalescence. The PDMS@Al patterned composite film surfaces provide heterogeneous wettability that promotes droplet collection as well as droplet roll-off, hence it has higher water collection rate compared with uniformly hydrophilic or hydrophobic surfaces.

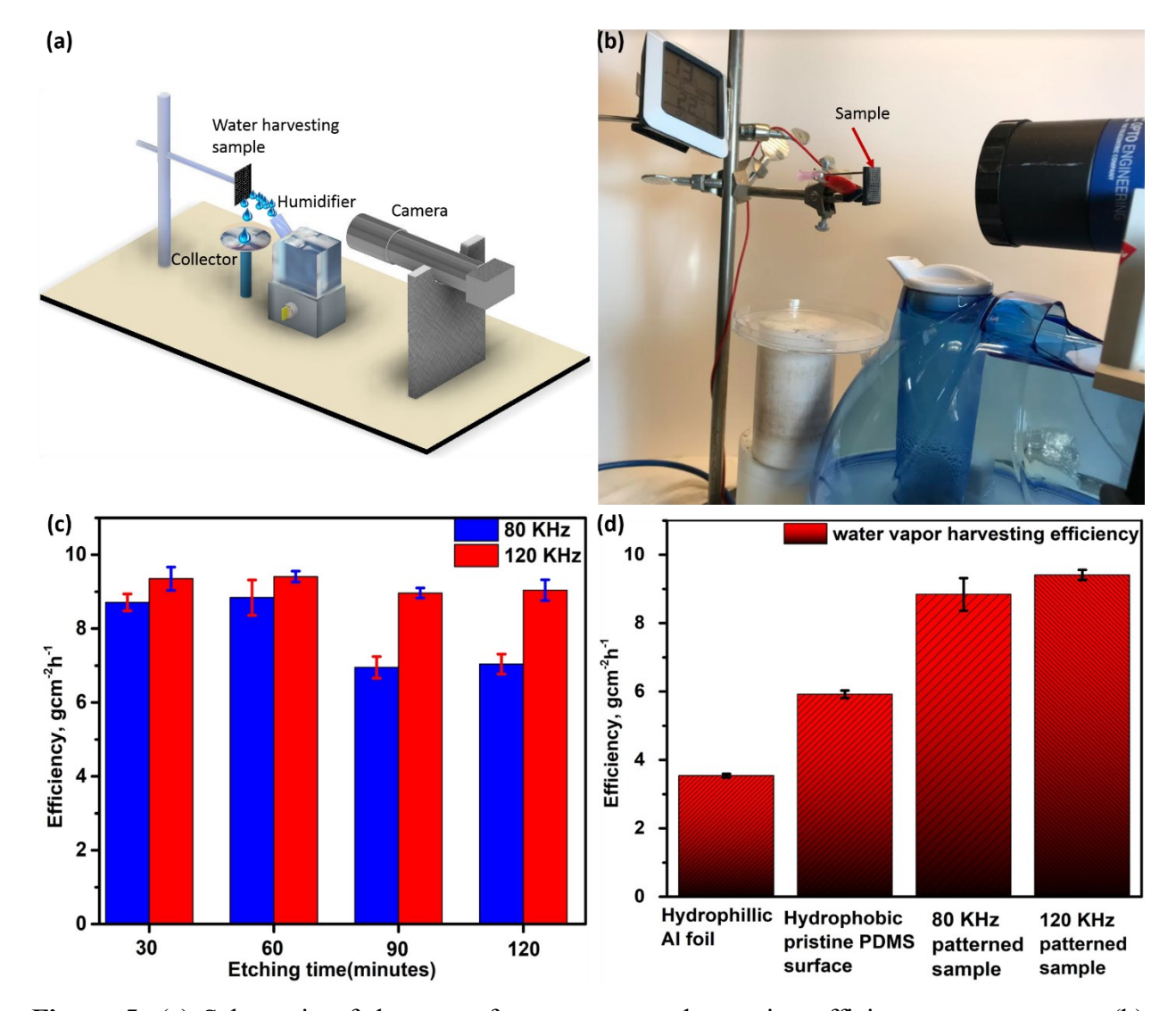


Figure 5: (a) Schematic of the setup for water vapor harvesting efficiency measurement. (b) Experimental setup showing the 120 KHz sample with one hour etching in front of the humidifier in the fume hood. (c) Water vapor harvesting efficiency comparison for both 80 KHz and 120 KHz samples under different etching time. (d)Comparison of the water vapor harvesting efficiency of the patterned samples with the hydrophilic Al foil and the hydrophobic pristine PDMS with one hour etching time.

The complete process of water harvesting on the composite surface was captured by a CCD camera and shown in Figure 6 and Supporting video S1-S3. In these figures and videos, the bright spots are the Al islands and the regions surrounding them are the PDMS. When the humidifier is activated, tiny droplets nucleated either on the PDMS valleys or on the island patterns and grew in sizes (Figure 6 (i-ii) and Supporting video S1). Then, as shown in Figure 6 (iii-iv) and Supporting video S2, the droplets, which condense at the regions surrounding the Al islands, move to the Al islands and merge into large droplets. The yellow arrows in Figure 6 (iii) indicate the directions the droplets move and Figure 6(iv) shows the large droplets after the merging. The force that drives the nucleated water droplets to the Al islands is related to the water wettability difference between

the Al islands and the PDMS as described by equation 5. According to equation 5, it can be inferred that the water wettability of the Al islands should be better than that of the PDMS, in order for the droplets to move in the observed direction. This serves as an evidence that wettability contrast on the composite surface has been achieved by the fabrication method. After the droplets moved to the Al island, the hydrophobic PDMS returned to a dry surface to capture the new incoming water vapor and the water harvesting process becomes continuous. Once the coalesced droplets that yet pinned on the Al islands become large enough such that its gravitational force overcomes the adhesion force, they roll off from the surface into the collector (Figure 6 (v) and Supporting video S3). It is also found that, falling droplet also captures the other droplets on its pathway and the surface becomes ready for another capture-collection-transportation cycle (Figure 6 (vi)).

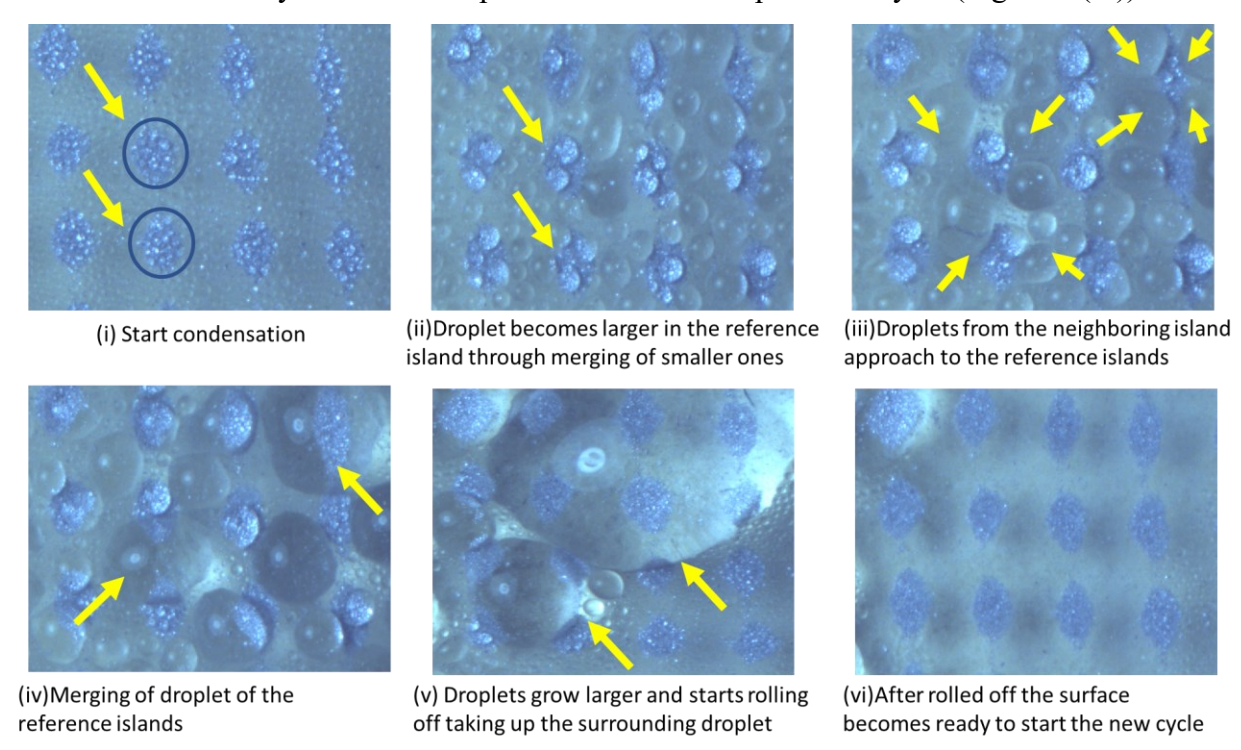


Figure 6: Demonstration of different steps of water harvesting process on the biomimetic composite surface. The average distance between the Al islands (bright spots in figure) is ∼1.2mm for reference of diemensions.

Using a test rig built in house (Figure S4), sliding angles were measured for samples made with both 120 KHz and 80 KHz and subjected to 1 hour of plasma etching. Microliter pipette was used to dispense the droplet of 40 uL and 50 uL respectively on both samples and the corresponding sliding angle measurements are shown in Table S4. For both volumes of water droplets, the 120 KHz sample has higher sliding angle than the 80 KHz one. With 120 KHZ input frequency, the average distance between Al islands is smaller than that at 80 KHZ, hence the number of islands per unit area increases as well as hydrophilicity and the sliding angle.

Finally, in order to test the performance of the biomimetic composite surface under highly humid environment, we have also measure their water harvesting efficiencies in a closed chamber where the maximum humidity was maintained at 92~94%. Figure S5 shows the etching time vs. water harvesting efficiency for both 80 KHz and 120 Khz samples in the closed environment. For 120

KHz samples the average efficiencies are 6.56, 7.025, 7.28 and 6.485 gcm⁻²h⁻¹ corresponding to etching time of 40, 60, 90 and 120 minutes respectively. On the other hand, for 80 KHz samples, the average values are 6.25, 6.49, 6.67 and 7.195 gcm⁻²h⁻¹. From the trend of data, it is observed that 120 KHz sample with 1.5 hour etching time shows improved performance compared with all other samples. The water harvesting efficiency is lower in environment with ultra-high humidity level than that in environment with low humidity level. As at above 90% humidity level, the fog from the humidifier is collected on the surface so rapidly that a thin water film rather than large droplets is quickly formed on the surface, which hinders the removal of the nucleated water and thus the refreshing of the surface for starting a new water harvesting cycle.

Conclusion

In this paper, Namib dessert beetle inspired compsite film with hydrophilic Al particle islands exposed on the surface of hydrophoblic PDMS substrate was fabricated by a facile two-step method consisting of acoustic patterning of the Al particles into islands in the PDMS matrix and then oxygen plasma etching to expose the Al islands on the surface. The resultant composite films have shown much higher water harvesting efficiency than purely hydrophobic or hydrophilic ones. Both the average height of the Al islands, as controlled by the oxygen plasma etching time, and the number of island per unit area, controlled by the excitation frequency of the acoustic actuators, affect the water harvesting efficiency. The as-developed film can be a versatile and energy-efficient solution to relieve the global water crisis.

Supporting Information

Heights (in μm) for different etching time of six islands to obtain the average height and determine the optimized the etching time (Table S1)

Water vapor harvesting efficiency for 80 KHz sample subjected to different etching time (Table S2)

Water vapor harvesting efficiency for 120 KHz sample subjected to different etching time (Table S3)

Sliding angles for samples made with 80 and 120 KHz and 1 hour etching (Table S4)

Representative SEM image of Al particles partially exposed at the surface of the PDMS-Al composite structure (Figure S1)

EDS mapping of the samples with etching and without etching (Figure S2)

SEM images of without plasma etching and excessive plama etching of the PDMS-Al composite surfaces (Figure S3)

Measurement method of the sliding angle using the protractor and ruler (Figure S4)

Water vapor harvesting efficiency comparison for both 80 KHz and 120 KHz samples under different etching time in highly humid environment (Figure S5)

Supporting video S1: Capture

Supporting video S2: Coalescence

Supporting video S3: Roll off

Acknowledgement

S. Hu and M Shahriar acknowledge the support by the U.S. National Science Foundation under Grant No. 1752378 and No. 1663509. The authors would like to thank Dr. Hui Hu and Mr. Chukwudum Eluchie for the help with water contact angle measurement, and thank Dr. Shan Jiang and Mr. Yifan Li for the help with oxygen plasma.

References

- 1.Overpeck, J. The Challenge of Hot Drought. *Nature* **2013**, 503, 350–351. DOI:10.1038/503350a
- 2. Mcgrath, S. G.; Sadler, R.; Fleming, K.; Tregoning, P.; Hinz, C.; Veneklaas, E. J. Tropical Cyclone and the Ecohydrology of Australia's Recent Continental-scale Drought, *Geophysical Research Letters* **2012**, 39, L03404. DOI:10.1029/2011GL050263
- 3. Dai, A. Increasing Drought Under Global Warming in Observations and Models. *Nature Climate Change*. **2013**, 3, 52-58. DOI:10.1038/nclimate1633
- 4. Trenberth, K. E.; Dai, A.; Van Der Schrier, G.; Jones, P.D., Barichivich, J.; Briffa, K. R.; Sheffield, J. Global Warming and Changes in Drought. *Nature Climate Change*. **2014**, 4, 17-22. DOI:10.1038/nclimate2067
- 5. Park, J. K.; Kim, S. Three-Dimensionally Structured Flexible Fog Harvesting Surfaces Inspired by Namib Desert Beetles. *Micromachines*, **2019**, 10(3), 201. DOI:10.3390/mi10030201
- 6. Fang, Y.; Xiong, L. General Mechanisms of Drought Response and their Application in Drought Resistance Improvement in Plants. *Cellular and Molecular Life Sciences*. **2015**, 72, 673-689. DOI:10.1007/s00018-014-1767-0
- 7. LaPotin, A.; Kim, H.; Rao, S. R.; Wang, E. N. Adsorption-based Atmospheric Water Harvesting: Impact of Material and Component Properties on System-level Performance. *Accounts of Chemical Research*. **2019**, 52(6), 1588-1597. DOI:10.1021/acs.accounts.9b00062
- 8. Al-Khayat, O.; Hong, J. K.; Beck, D. M.; Minett, A. I.; Neto, C. Patterned Polymer Coatings Increase the Efficiency of Dew Harvesting. *ACS Applied Materials & Interfaces*. **2017**, 9(15), 13676-13684. DOI:10.1021/acsami.6b16248
- 9. Brown, P. S.; Bhushan, B. Bioinspired Materials for Water Supply and Management: Water Collection, Water Purification and Separation of Water from Oil. *Philosophical Transactions of the Royal Society A: Mathematical, Physical and Engineering Sciences.* **2016**, 374(2073), 20160135. DOI:10.1098/rsta.2016.0135

- 10. Zhang, S.; Huang, J.; Chen, Z.; Lai, Y. Bioinspired Special Wettability Surfaces: From Fundamental Research to Water Harvesting Applications. *Small.* **2017**, 13(3), 1602992. DOI:10.1002/smll.201602992
- 11. Pinchasik, B. E.; Kappl, M.; Butt, H. J. Small Structures, Big Droplets: The Role of Nanoscience in Fog Harvesting. *ACS Nano.* **2016**, 10(12), 10627-10630. DOI:10.1021/acsnano.6b07535
- 12. Bai, H.; Lin, W.; Jie, J.; Ruize, S; Yongmei, Z.; Lei, J. Efficient Water Collection on Integrative Bioinspired Surfaces with Star-Shaped Wettability Patterns. *Advanced Materials*, **2014**, 26(29), 5025-5030. DOI:10.1002/adma.201400262
- 13. Zhang, L.; Wu, J.; Hedhili, M. N.; Yang, X.; Wang, P. Inkjet Printing for Direct Micropatterning of a Superhydrophobic Surface: Toward Biomimetic Fog Harvesting Surfaces. *Journal of Materials Chemistry A.* **2015**, 3, 2844-2852. DOI:10.1039/C4TA05862C
- 14. Kim, N.K.; Kang, D.H.; Eom H.; Kang, H.K. Biomimetic Fog harvesting Surface by Photo-Induced Micro-patterning of Zinc-oxide Silver Hierarchical Nanostructures, *Applied Surface Science*, **2019**, 470, 161-167. DOI:10.1016/j.apsusc.2018.11.132
- 15. Parker, A. R.; Lawrence, C. R.; Water Capture by a Desert Beetle. *Nature*, **2001**, 414, 33-34. DOI:10.1038/35102108
- 16. Hamilton, W. J.; Seely, M. K. Fog Basking by the Namib Desert Beetle, Onymacris unguicularis. *Nature*, **1976**, 262, 284-285. DOI:10.1038/262284a0
- 17. Nørgaard, T.; Dacke, M.; Fog-Basking Behaviour and Water Collection Efficiency in Namib Desert Darkling beetles. *Frontiers in zoology.* **2010**, 7, 1-8. DOI:10.1186/1742-9994-7-23
- 18. Zhu, H.; Huang, Y.; Lou, X.; Xia, F. Beetle Inspired Wettable Materials: from Fabrications to Applications, *Materials Today Nano*, **2019**, 6, 100034. DOI:10.1016/j.mtnano.2019.100034
- 19. Wang, Y.; Zhang, L.; Wu, J.; Hednili, N. M.; Wang, P. A Facile Strategy for the Fabrication of a Bioinspired Hydrophilic-superhydrophobic Patterned Surface for Highly Efficient Fogharvesting, *Journal of Materials Chemistry A*, **2015**, 3, 18963. DOI:10.1039/C5TA04930J
- 20. Lichade, K. M.; Hu, S.; Pan, Y.; Two-Photon Polymerization of Anisotropic Composites Using Acoustic Streaming, *Manufacturing Letters*, **2022**, 31, 110-115. DOI:10.1016/j.mfglet.2021.09.001
- 21. Wu, J. Acoustical Tweezers. *The Journal of the Acoustical Society of America*. **1991**, 89, 2140-2143. DOI:10.1121/1.400907
- 22. Shi, J.; Ahmed, D.; Mao, X.; Lin, S.C.S.; Lawit, A; Haung, T.J. Acoustic Tweezers: Patterning Cells and Microparticles Using Standing Surface Acoustic Waves (SSAW), *Lab on a Chip*, **2009**, 9, 2890-2895. DOI:10.1039/B910595F

- 23. Yu, Z.; Yun, F. F.; Wang, Y.; Yao, L.; Dou, S.; Liu, K. Desert Beetle-Inspired Superwettable Patterned Surfaces for Water Harvesting, *Small*, **2017**, 13(36), 1-6. DOI:10.1002/smll.201701403
- 24. You, H.; Zhang, Y.; Hu, Y.; Song, Y.; Xue, C.; Ji, S.; Li, R.; Li, L.; Li, J.; Wu, D.; Chu, J. Kirigami Structures of Shape Memory Polymer by Femtosecond Laser Scribing and Constrained Heating. *Advance Material Technologies*, **2021**, 6 (7), 2100200. DOI:10.1002/admt.202100200
- 25.Su, Y.; Chen, L.; Jiao, Y.; Zhang, J.; Li, C.; Zhang, Y.; Zhang, Y. Hierarchical Hydrophilic/Hydrophobic/Bumpy Janus Membrane Fabricated by Femtosecond Laser Ablation for Highly Efficient Fog Harvesting. *ACS Applied Materials & Interfaces.* **2021**, 13 (22), 26542-26550. DOI:10.1021/acsami.1c02121
- 26. Gosse, C.; Croquette, V. Magnetic Tweezers: Micromanipulation and Force Measurement at the Molecular Level. *Biophysical Journal*, **2002**, 82(6), 3314-3329. DOI:10.1016/S0006-3495(02)75672-5
- 27. Perkins, T. T. Optical Traps for Single Molecule Biophysics: A Primer. *Laser & Photonics Reviews*, **2009**, 3(1-2), 203-220. DOI:10.1002/lpor.200810014
- 28. Ashkin, A.; Dziedzic, J. M. Optical Trapping and Manipulation of Viruses and Bacteria. *Science*. **1987**, 235(4795), 1517-1520. DOI:10.1126/science.3547653
- 29. Wu, M. C. Optoelectronic Tweezers. *Nature Photonics*. **2011**, 5, 322-324. DOI:10.1038/nphoton.2011.98
- 30. Wang, K.; Schonbrun, E.; Steinvurzel, P.; Crozier, K. B. Trapping and Rotating Nanoparticles Using a Plasmonic Nano-tweezer with an Integrated Heat Sink. *Nature communications*. **2011**, 2, 1-6. DOI:10.1038/ncomms1480
- 31. Llewellyn-Jones, T. M.; Drinkwater, B. W.; Trask, R. S. 3D Printed Components with Ultrasonically Arranged Microscale Structure. *Smart Materials and Structures*, **2016**, 25 no. 2, 02LT01. DOI:10.1088/0964-1726/25/2/02LT01
- 32. Lu, L.; Tang, X.; Hu, S.; Pan, Y. Acoustic Field-assisted Particle Patterning for Smart Polymer Composite Fabrication in Stereolithography. *3D Printing and Additive Manufacturing* 5, **2018**, no. 2, 151-159. DOI:10.1089/3dp.2017.0157
- 33. Ozcelik, A.; Rufo, J.; Guo, F.; Gu, Y.; Li, P.; Lata, J., Huang, T.J., Acoustic Tweezers for the Life Sciences. *Nature Methods*, **2018**,15, 1021–1028. DOI:10.1038/s41592-018-0222-9.
- 34. Marzo, A.; Caleap, M.; Drinkwater, B.W. Acoustic Virtual Vortices with Tunable Orbital Angular Momentum for Trapping of Mie Particles. *Physical Review Letters*, **2018**, 120(4), 044301. DOI:10.1103/PhysRevLett.120.044301

- 35. Oberti, S.; Neild, A.; Dual, J. Manipulation of Micrometer Sized Particles within a Micromachined Fluidic Device to Form Two-dimensional Patterns Using Ultrasound. *Journal of Acoustical Society of America*, **2007**, 121(2), 778–785. DOI:10.1121/1.2404920
- 36. Tian, Z.; Wang, Z.; Zhang, P.; Naquin, T. D.; Mai, J.; Wu, Y.; Yang, S.; Gu, Y.; Bachman, H.; Liang, Y.; Yu, Z.; Huang, T. J. Generating Multifunctional Acoustic Tweezers in Petri Dishes for Contactless, Precise Manipulation of Bioparticles, *Science Advances*, **2021**, 7, 1-6. DOI:10.1126/sciadv.abb0494
- 37. Junfei, L.; Shen, C.; Huang, T. J.; Cummer, S.A. Acoustic Tweezer with Complex Boundary-Free Trapping and Transport Channel Controlled by Shadow Waveguides. *Science Advances*, **2021**,7, no. 34 eabi5502. DOI:10.1126/sciadv.abi5502
- 38.Ye, Y.; Ma, T.; Li, S.; Zhang, Q.; Huang, J.; Liu, Y.; Zhuang, J. Self-navigated 3d Acoustic Tweezers in Complex Media based on Time Reversal, *Research*, **2021**, Article ID: 9781394. DOI:10.34133/2021/9781394
- 39. Marzo, A.; Drinkwater, W.B. Holographic Acoustic Tweezers. *Proceedings of the National Academy of Sciences*, **2019**, 116(1), 84-89. DOI:10.1073/pnas.1813047115
- 40. Guo, F.; Mao, Z.; Chen, Y.; Xie, Z.; Lata, J. P.; Li, P.; Ren, L.; Liu, J.; Yang, J.; Dao, M.; Suresh, S.; Huang, T. J. Three-Dimensional Manipulation of Single Cells Using Surface Acoustic Waves. *Proceedings of the National Academy of Science*, **2016**, 113(6), 1522-1527. DOI:10.1073/pnas.1524813113
- 41. Bruus, H. Acoustofluidics 7:The Acoustic Radiation Force on Small Particles, *Lab Chip*, **2012**, 12, 1014-1021. DOI:10.1039/C2LC21068A
- 42. Koklu, M.; Sabunchu, A.C.; Beskok, A. Acoustophoresis in Shallow Microchannels, *Journal of Colloid Interface Science*, **2010**, 351(2), 407-414. DOI:10.1016/j.jcis.2010.08.029
- 43. Muller, P.B.; Barnkob, R.; Jensen, M. J. H.; Bruus, H. A Numerical Study of Microparticle Acoustophoresis Driven by Acoustic Radiation Forces and Streaming-Induced Drag Forces. *Lab on a Chip*, **2012**, 12(22), 4617-4627. DOI:10.1039/C2LC40612H
- 44. Dai, X.; Sun, N.; Nielsen, S.O.; Stogin, B.B.; Wang, J.; Yang, S.; Wong, T.S. Hydrophilic Directional Slippery Rough Surfaces for Water Harvesting. *Science Advances*, **2018**, 4. eaaq091. DOI:10.1126/sciadv.aaq0919
- 45. Monga, D.; Guo, Z.; Shan, L.; Taba, S.A.; Sarma, J.; Dai, X. Quasi-Liquid Surfaces for Sustainable High-Performance Steam Condensation, *ACS Applied Materials & Interfaces*, **2022**, 14 (11), 13932-13941. DOI:10.1021/acsami.2c00401

46. Guo, Z.; Zhang, L.; Monga, D.; Stone, H. A.; Dai, X., Hydrophilic Slippery Surface Enabled Coarsening Effect for Rapid Water Harvesting. *Cell Reports Physical Science*, **2021**, 2(4), 100387. DOI:10.1016/j.xcrp.2021.100387.

48. Hillborg, H.; Ankner, J.F.; Gedde, U. W.; Smith, G. D.; Yasuda, H.K.; Wikström, K. Crosslinked Polydimethylsiloxane Exposed to Oxygen Plasma Studied by Neutron Reflectometry and Other Surface Specific Techniques. *Polymer*, **2000**, 41(18), 6851-6863. DOI:10.1016/S0032-3861(00)00039-2.